# Supporting Information

## Nanostructured, Mn-doped $V_2O_5$ Cathode Material Fabricated from Layered Vanadium Jarosite

Hongmei Zeng,[*,†,‡,§] Deyu Liu,[†,§] Yichi Zhang,[†] Kimberly A. See,[†] Young-Si Jun,[†] Guang Wu,[†] Jeffrey A. Gerbec,[⊥] Xiulei Ji,[Δ] and Galen D. Stucky[*,†,⊥]

[†]Department of Chemistry & Biochemistry, University of California, Santa Barbara CA 93106-9510 USA
[‡]College of Chemistry, Sichuan University, Chengdu, 610064, China

[⊥]Mitsubishi Chemical Center for Advanced Materials, University of California, Santa Barbara CA 93106-5150, USA
[Δ]Department of Chemistry, Oregon State University, Corvallis OR 97331 USA

*G. D. Stucky, E-mail: stucky@chem.ucsb.edu
*H. Zeng, E-mail: zenghongmei@scu.edu.cn

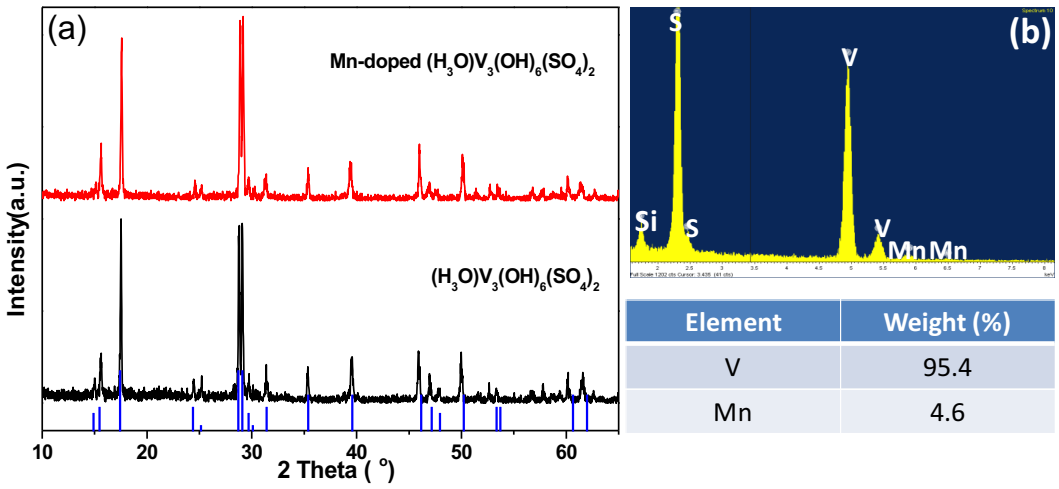


| Element | Weight (%) |
|---|---|
| V | 95.4 |
| Mn | 4.6 |

**Figure S1.** (a) XRD patterns of different microwave-assisted reaction products, the standard XRD pattern of V-jarosite without doping is shown on the bottom; (b) EDX spectrum of the Mn-doped $(H_3O)V_3(OH)_6(SO_4)_2$.

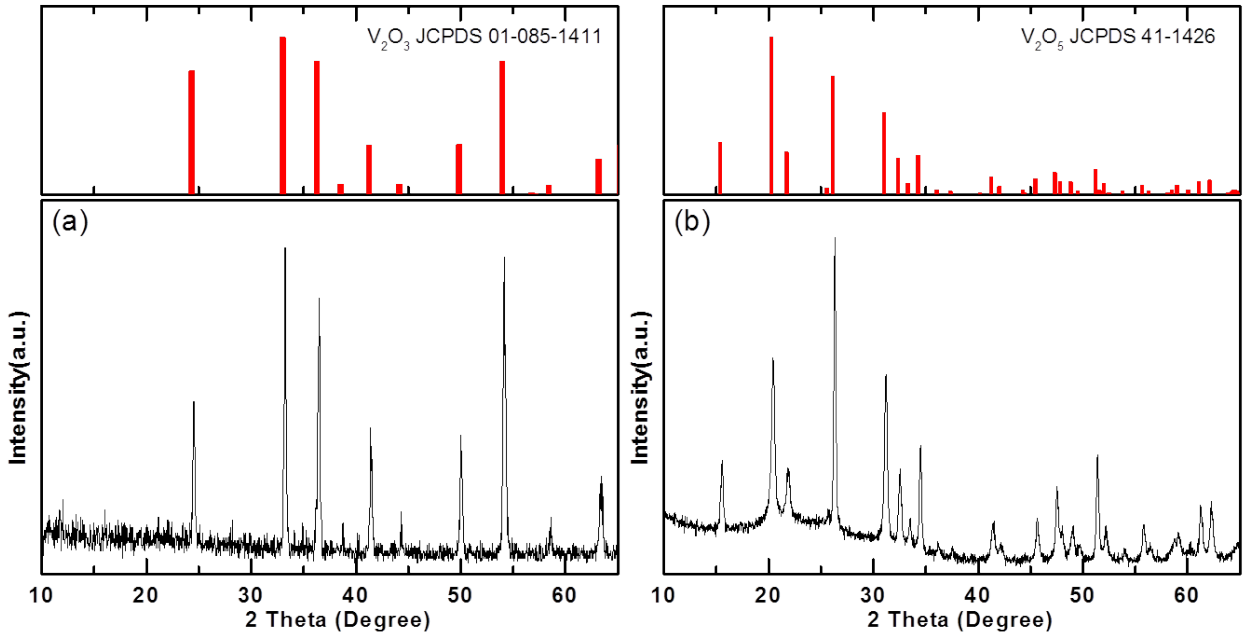


**Figure S2.** XRD pattern of: (a) $V_2O_3$ sample (prepared by annealing the jarosite); (b) $V_2O_5$ sample (prepared by annealing the $V_2O_3$). Upper panels: standard XRD pattern of $V_2O_3$ and $V_2O_5$ corresponding with (a) and (b) respectively.

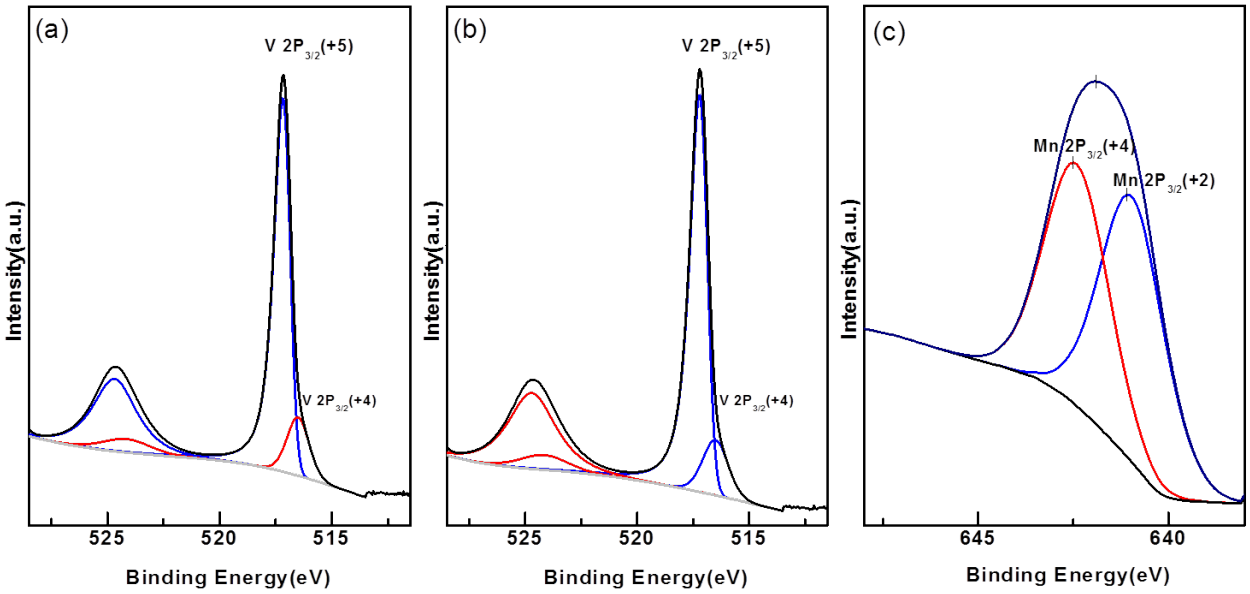


**Figure S3.** Curve fitting of the $V_{2p}$ XPS spectra of (a) undoped $V_2O_5$ and (b) Mn-doped $V_2O_5$ and (c) the $Mn_{2p3/2}$ band of doped $V_2O_5$. The XPS data suggest the coexistence of $Mn^{2+}$ and $Mn^{4+}$. $Mn^{2+}$ atoms have the significant larger ionic radius than $V^{5+}$, while $Mn^{4+}$ has a very similar ionic radius to $V^{5+}$ and thus we attribute the impact of Mn doping to the $V_2O_5$ crystal lattice derives from the $Mn^{2+}$.

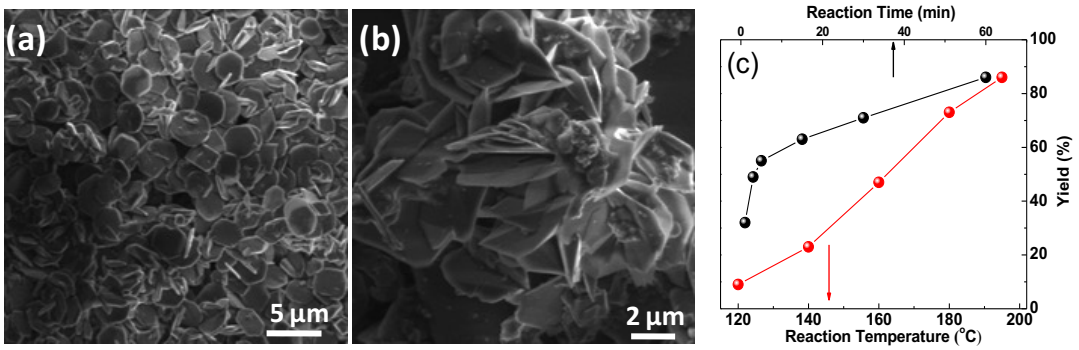


**Figure S4.** SEM images of the products : (a) $(H_3O)V_3(OH)_6(SO_4)_2$ (prepared at 195 $^oC$ for 1h); (b) $(H_3O)V_3(OH)_6(SO_4)_2$ (prepared at 195 $^oC$ for 1min); and (c) the production yield of $(H_3O)V_3(OH)_6(SO_4)_2$ prepared at different time and temperature (compared to the complete stoichiometric conversion).

In order to understand the time and temperature dependence of vanadium jarosite formation, we investigated a series of synthesis reaction temperatures (Figure S3c). Below 120 $^oC$, the reaction rate is slowed down probably due to the activation energy requirement from the redox reaction. The vanadium jarosite particles exhibit a flake-like morphology that tends to grow into larger polycrystals with extended reaction time (Figure S3**a** and **b**).

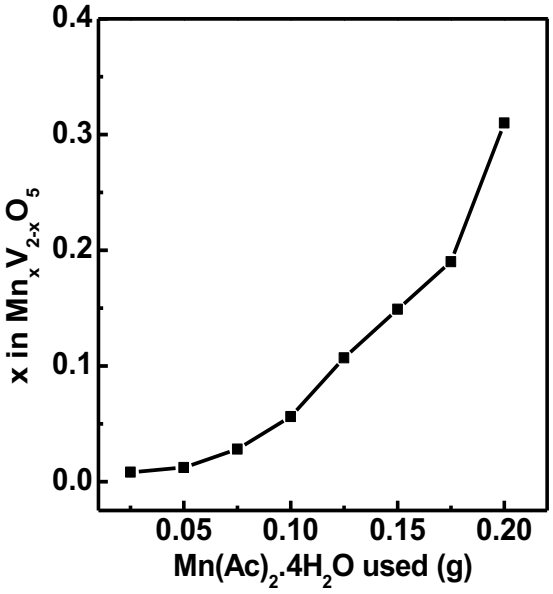


**Figure S5.** Chemical composition of the products as a function of the amount of $Mn(Ac)_2{\cdot}4H_2O$ used in each synthesis.

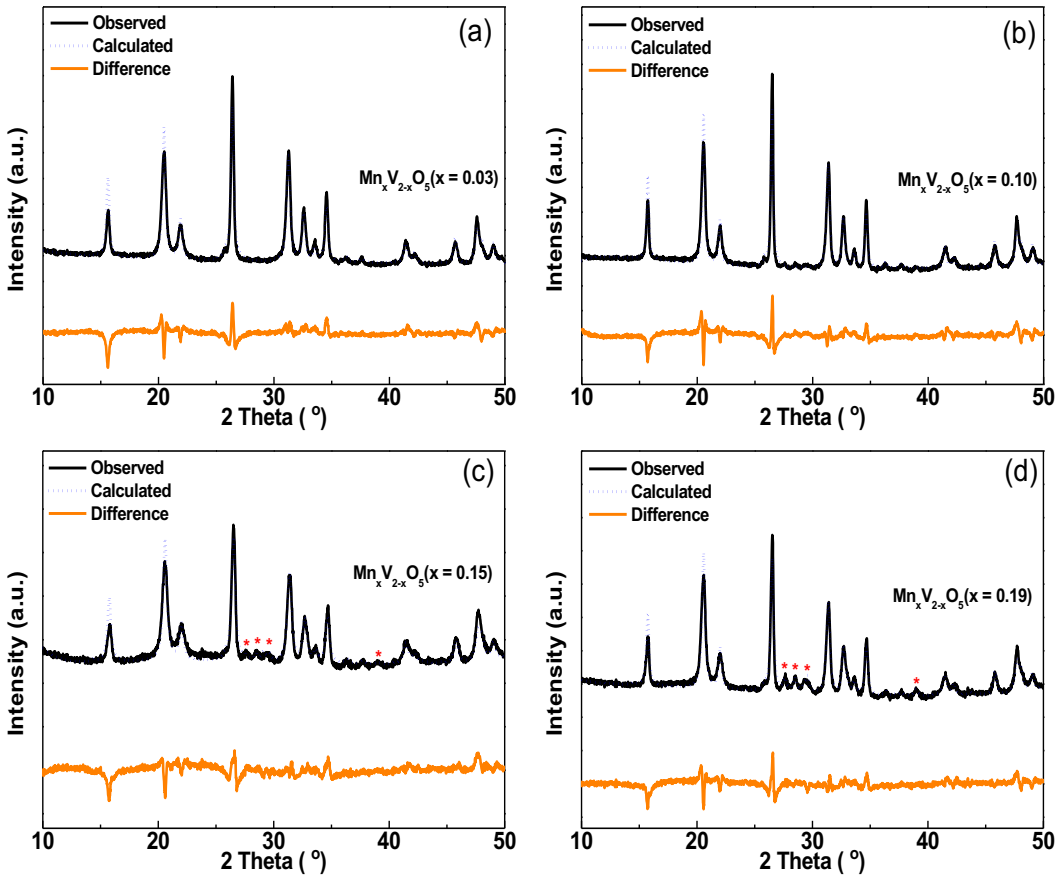


**Figure S6.** Rietveld refined XRD patterns of the $Mn_xV_{2-x}O_5$: (a) x = 0.03; (b) x = 0.10; (c) x = 0.15 and (d) x = 0.19.

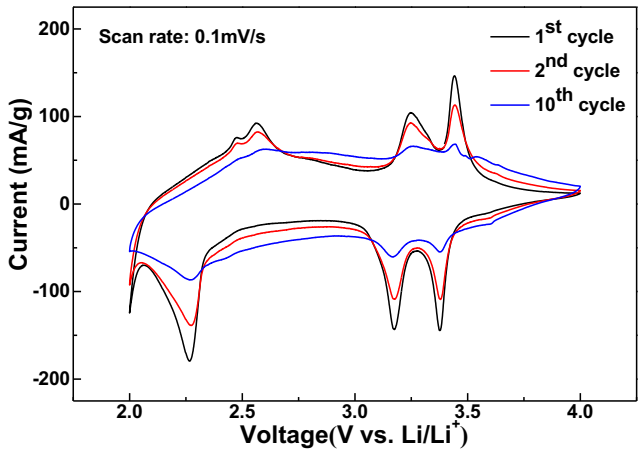


**Figure S7.** Cyclic voltammetry (CV) of the $V_2O_5$ electrode in the voltage range between 2.05 and 4.0 V (vs. $Li^+/Li$) at a scan rate of 0.1 $mVs^{-1}$.

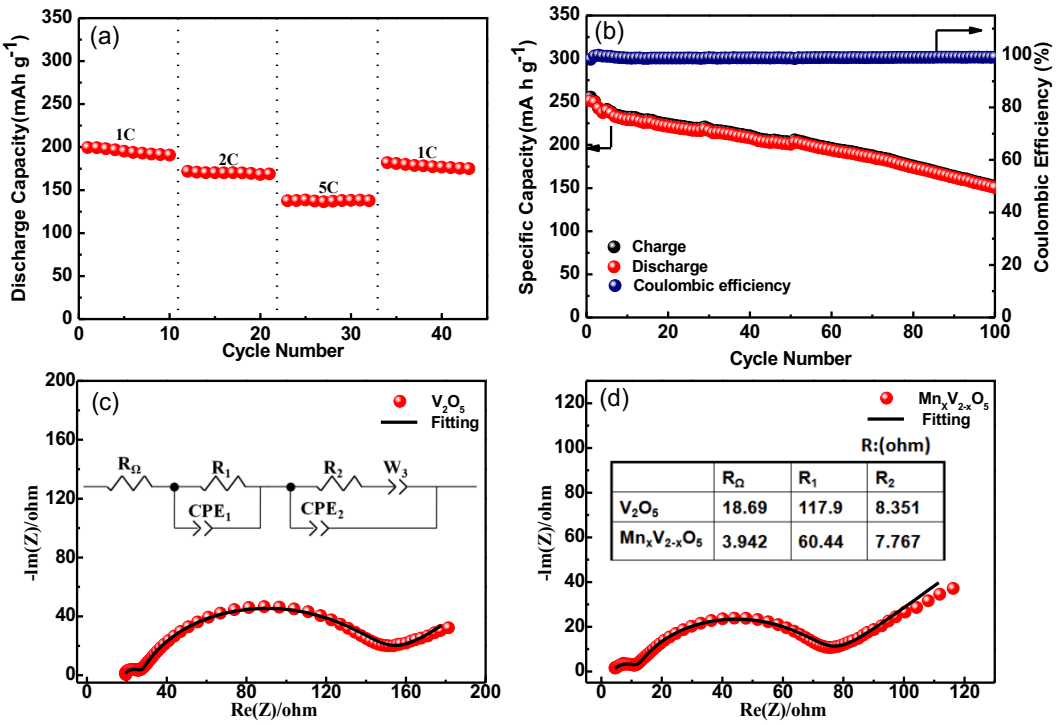


| | $R_\Omega$ | $R_1$ | $R_2$ |
|---|---|---|---|
| $V_2O_5$ | 18.69 | 117.9 | 8.351 |
| $Mn_xV_{2-x}O_5$ | 3.942 | 60.44 | 7.767 |

**Figure S8.** The electrochemical performances of the undoped and Mn-doped $V_2O_5$ electrode in the voltage range between 2.05 and 4.0 V (vs. Li): (a) rate performance of the M19 electrode; (b) cycling performance and Coulombic efficiency of the M01 electrode at a rate of 300 mA·g$^{-1}$; (c) Nyquist plots of the undoped $V_2O_5$ electrode; (d) Nyquist plots of the M01 electrode. Inset of (c) is the equivalent circuit used for fitting the Nyquist plots, and inset of (d) is the values for undoped $V_2O_5$ and M01 samples from fitting of EIS plots.

**Table S1.** The influence of doping level on the electric components in the equivalent circuit used to fit the EIS data

| Sample# | *Doping level (at% Mn)* | $R_\Omega$ (Ω) | $R_1$ (Ω) | $R_2$ (Ω) |
|---|---|---|---|---|
| M01 | 1 | 3.942 | 60.44 | 7.767 |
| M06 | 6 | 4.565 | 63.35 | 6.095 |
| M10 | 10 | 35.19 | 66.14 | 3.677 |
| M19 | 19 | 6.057 | 171.1 | 25.58 |
| Pristine $V_2O_5$ | 0 | 18.69 | 117.9 | 8.351 |

Figure S8 (c) and (d) show the EIS analysis of undoped and Mn-doped $V_2O_5$ cathodes. Both impedance plots show two separate semicircles in the high-frequency range and a sloped line in

the low-frequency region. At high frequency, the semicircle corresponds to the transport resistance of lithium ions through the solid electrolyte interface (SEI) layer. The second semicircle at intermediate frequency corresponds to the charge transfer reaction at the electrode/electrolyte interface. At low frequency, a slanted line corresponds to the transportation of lithium ions within the solid material. A simplified equivalent circuit model (inset of Figure S6c) can be used to describe the frequency dependence of these two samples. The calculated parameters are listed in inset table of Figure S6d. In this circuit, $R_\Omega$ represents the Ohmic resistance of the electrode system, which is from the electrolyte and the cell components. $R_1$ represents the resistance coming from the lithium ion diffusion through the interface between the surface layer of the $Mn_xV_{2-x}O_5$ electrode/electrolyte (including SEI layer and surface-modification layer). $CPE_1$ is the constant phase-angle element depicting the non-ideal capacitance of the surface layer. $R_2$ refers to the charge transfer resistance. $W_3$ represents the Warburg impedance describing the lithium ion diffusion in the bulk material, and $CPE_2$ is the constant phase-angle element depicting the non-ideal capacitance arising due to additional unknown electrochemical processes.

Table S1 shows the fitted components of EIS measurements from samples with different doping amounts. A significant reduction of both $R_1$ and $R_2$ is observed at doping levels relative to the undoped $V_2O_5$. Specifically, $R_1$ decreases by ~50% compared with the undoped $V_2O_5$, which suggests more facile $Li^+$ diffusion. $R_2$ decreases with increasing doping level. Reduction of this resistance suggests better electronic conductivity inside the cathode, which agrees with the commonly agreed increases in electronic conductivity of semiconductors with higher doping levels as the result of higher carrier density. For the over-doped sample M19, all resistances are significantly larger than those samples of the optimized doped level. This behavior is due to the formation of the inactive phase $MnV_2O_6$.